Characteristics of a Convective-Scale Weather Forecasting System for the European Arctic

Malte Müller, Yurii Batrak, Jørn Kristiansen,
Morten A. Ø. Køltzow, and Gunnar Noer

Norwegian Meteorological Institute, Oslo, Norway

Anton Korosov

Nansen Environmental and Remote Sensing Center, Bergen, Norway

(Manuscript received 7 July 2017, in final form 21 September 2017)

ABSTRACT

In this study a 1-yr dataset of a convective-scale atmospheric prediction system of the European Arctic (AROME-Arctic) is compared with the ECMWF's medium-range forecasting, ensemble forecasting, and reanalysis systems, by using surface and radiosonde observations of wind and temperature. The focus is on the characteristics of the model systems in the very short-term forecast range (6–15 h), but without a specific focus on lead-time dependencies. In general, AROME-Arctic adds value to the representation of the surface characteristics. The atmospheric boundary layer thickness, during stable conditions, is overestimated in the global models, presumably because of a too diffusive turbulence scheme. Instead, AROME-Arctic shows a realistic mean thickness compared to the radiosonde observations. All models behave similarly for the upper-air verification and surprisingly, as well, in forecasting the location of a polar low in the short-range forecasts. However, when comparing with the largest wind speeds from ocean surface winds and at coastal synoptic weather stations during landfall of a polar low, AROME-Arctic shows the most realistic values. In addition to the model intercomparison, the limitation of the representation of sea ice and ocean surface characteristics on kilometer scales are discussed in detail. This major challenge is illustrated by showing the rapid drift and development of sea ice leads during a cold-air outbreak. As well, the available sea surface temperature products and a high-resolution ocean model result are compared qualitatively. New developments of satellite products, ocean–sea ice prediction models, or parameterizations, tailored toward high-resolution atmospheric Arctic prediction, are necessary to overcome this limitation.

1. Introduction

Over the past few decades the Arctic has warmed more than any other region in the world, with profound socioeconomic consequences. As a result, there is a growing demand for accurate Arctic weather predictions, which puts great expectations on our current global and regional forecasting systems (Emmerson and Lahn 2012; Jung et al. 2016). There are many challenges for Arctic weather prediction, for example, the sparse observation network, atmospheric data assimilation, the representation of sea ice, and the high-latitude representation of many subgrid-scale parameterizations (WMO-PPP 2013; Vihma et al. 2014).

Global weather forecasting systems have a horizontal resolution of around 10 km and will in the near future approach convective permitting scales, by reducing the grid spacing below ~4 km. Recent studies, based on global or pan-Arctic systems, have shown that significant progress has been made in recent decades in improving forecasting skill, the representation of uncertainties, and forecast analyses in the Arctic region (Jung and Leutbecher 2007; Jung and Matsueda 2016; Bauer et al. 2016; Bromwich et al. 2016; Hines and Bromwich 2017). Furthermore, as is shown for the polar low representation in global analyses (Zappa et al. 2014), global systems are already able to resolve to some extent the mesoscale high-latitude dynamics.

ᵃ Denotes content that is immediately available upon publication as open access.

Corresponding author: Malte Müller, maltem@met.no

Regional model systems already have kilometer-scale resolution and, thus, start to resolve convective atmospheric processes (e.g., Seity et al. 2011). Recent studies showed the use and advances of high-resolution regional versus coarser-resolution global model systems (Gutjahr et al. 2016; Moore et al. 2016; Smirnova and Golubkin 2017). However, to our knowledge, there have been no detailed studies analyzing the characteristics of a convection-permitting high-resolution system for the Arctic region. In the European Arctic the convective-scale weather prediction system Applications of Research to Operations at Mesoscale (AROME-Arctic) has been in operation since November 2015. Forecast analyses are derived via a 3DVAR data assimilation scheme and observations from various sources, including synoptic, radiosonde, airplane, and satellite data. It is the main Arctic weather forecasting tool used by the Norwegian Meteorological Institute, which has national and international responsibilities for weather, sea ice, and ocean prediction in large parts of the European Arctic. The recent entry into service of the operational AROME-Arctic model is intended to improve the representation of physical phenomena and to tackle challenges related to the observation (in situ and remote sensing) network and the associated data assimilation methodologies, which all present unique challenges for polar regional weather prediction. AROME-Arctic is one of the core models of the Year of Polar Prediction (YOPP) and further, the AROME model system will be central to the coming high-resolution Arctic reanalysis, as part of the Copernicus Climate Change Service.

The purpose of the present study is to extend previous studies of Arctic weather prediction by comparing a convective-scale system with coarser-resolution model systems from the European Centre for Medium-Range Weather Forecasts (ECMWF) Integrated Forecast System (IFS). We analyze a 1-yr record of very short-range forecasts (6–15 h) in order to assess the model's ability to resolve characteristics of temperature and wind at the surface, the boundary layer, and in the upper troposphere and lower stratosphere. Moreover, the short-range predictability and representation of a polar low are assessed. With near-surface wind speeds in excess of $15\,\mathrm{m\,s^{-1}}$, polar lows are the most intense systems in the family of polar mesoscale cyclones. These storms are smaller and more transient than the more familiar and predictable synoptic-scale weather systems. Residing poleward of the main polar front, polar lows can potentially be a hazard to high-latitude marine operations (e.g., shipping, gas, and oil platforms) and also affect land transport and aviation.

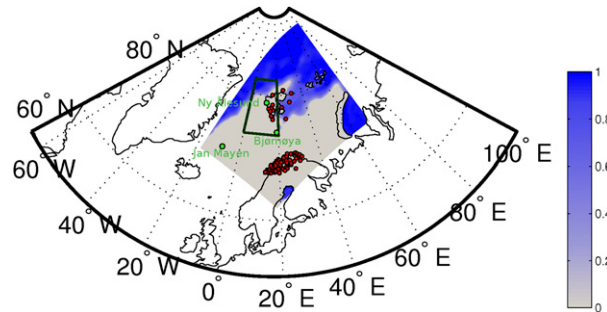The paper is organized as follows. In section 2 we give a brief description of the model systems. An

FIG. 1. The model domain is shown by a color-contoured field of sea ice concentration (5 Mar 2016). Furthermore, surface observations and radiosondes used for the statistical verification are shown by red and green dots, respectively. The dark green box indicates the area used for the CAO index computation.

evaluation against surface and radiosonde observations is given in section 3. In section 4 a detailed study of a polar low event is provided and in section 5 we describe the current challenges in the representation of sea ice and ocean characteristics in the high-resolution model system. A summary and a conclusion are provided in section 6.

2. Models

A regional model, the convective-scale regional AROME-Arctic, and three configurations of ECMWF's global model system, the deterministic (HRES), ensemble (ENS), and reanalysis (ERA-Interim) (Bauer et al. 2013; Dee et al. 2011), are used in the present study.

AROME-Arctic is a regional high-resolution forecasting system for the European Arctic with a horizontal resolution of 2.5 km and 65 vertical levels (Figs. 1 and 2). The model is primarily based on the High Resolution Limited Area Model (HIRLAM)–ALADIN Research on Mesoscale Operational NWP in Euromed (HARMONIE) AROME configuration (version 38h1.2; Bengtsson et al. 2017). More details on the model system are given in Seity et al. (2011) and on the Nordic setup [AROME-Meteorological Cooperation on Operational Numerical Weather Prediction (AROME-MetCoOp)] in Müller et al. (2017). AROME-Arctic is currently very similar to the AROME-MetCoOp setup and a large set of conventional and satellite observations are assimilated by a 3DVAR and optimal interpolation data assimilation systems, for upper-air and surface observations, respectively. The AROME-Arctic model is forced by HRES at the lateral and upper boundaries. The coupling zone in which the AROME-Arctic model is relaxed toward the large-scale coupling model is eight
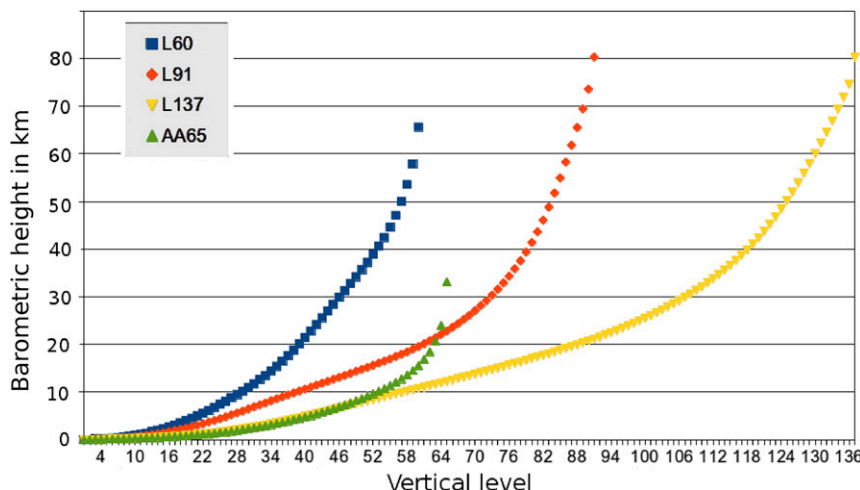
FIG. 2. The distribution of vertical levels in the forecasting systems. The *x* axis is the level number starting with the level closest to the surface. The *y* axis represents the standard altimetric height (km). AA65 refers to the 65 levels of AROME-Arctic. L137, L91, and L60 refer to the vertical levels of HRES, ENS, and ERA-Interim, respectively.

grid points wide in the horizontal and the eight top levels in the vertical (Davies 1976).

Because of the delayed availability of HRES forecasts, the analysis times of the HRES forecasts, which are used as boundaries, are 6 h earlier than the actual forecasts. The sea surface temperature (SST) is regridded from the HRES, which, in turn, is based on the Operational Sea Surface Temperature and Sea Ice Analysis (OSTIA; Donlon et al. 2012) from the Met Office. Sea ice concentrations are obtained from the Ocean and Sea Ice Satellite Application Facilities (OSI-SAF; Tonboe et al. 2016). The surface temperature over sea ice is taken once from HRES (cold start) and is subsequently modeled by a 1D sea ice model (Y. Batrak et al. 2017, unpublished manuscript, hereafter BKH).

A detailed description of the ECMWF model systems can be found in Bauer et al. (2013) and Dee et al. (2011). ERA-Interim is a fixed-model system with a model resolution of around 80 km and 60 vertical levels (Fig. 2). HRES and ENS model systems are under constant development and a major change within our analysis period occurred 8 March 2016, where the linear reduced Gaussian grid was changed to a cubic reduced Gaussian grid. With this change the spectral truncation is unchanged but the gridpoint space resolution is increased to more accurately represent the physical processes and advection. Thus, in HRES and ENS the horizontal resolutions changed from 18 to 9 km and 36 to 18 km, respectively. The number of vertical levels is 137 in HRES and 91 in ENS (Fig. 2). A second change occurred 22 November 2016 (from version 41r2 to 43r1), with the main modifications in the ocean component

(http://www.ecmwf.int/en/forecasts/documentation-and-support/changes-ecmwf-model). Note, from ENS we are using the control run only.

3. Statistical verification

A statistical verification over a 1-yr period (1 December 2015–30 November 2016) is performed. The focus of this study is on verification of temperature and wind only. The characteristics of temperature and wind vary considerably from season to season (Fig. 3). In between October and May the variability of temperature and wind is high. Surface observations for example at Bjørnøya, an island between the Norwegian mainland and the Svalbard Archipelago, show abrupt temperature changes of up to 10 K and wind maxima of around 20 m s^{-1}. Instead, in the months between May and September this variability is significantly smaller.

The larger atmospheric variability during the winter months is mainly caused by the increased north–south temperature gradient and the alternation of northerly and southerly winds. In this regard, an important winter phenomenon is cold-air outbreaks (CAO). During CAOs cold air masses are transported from ice-covered areas toward lower latitudes and sea-ice-free areas. For illustration we compute the CAO index from 6-h forecasts of the AROME-Arctic model (Fig. 3). The index is defined by the difference between the 850-hPa potential temperature and surface skin temperature (Papritz et al. 2015), and integrated over the area west of the Svalbard Archipelago. This area is indicated in Fig. 1 by a green box. The observed temperature and wind time series,
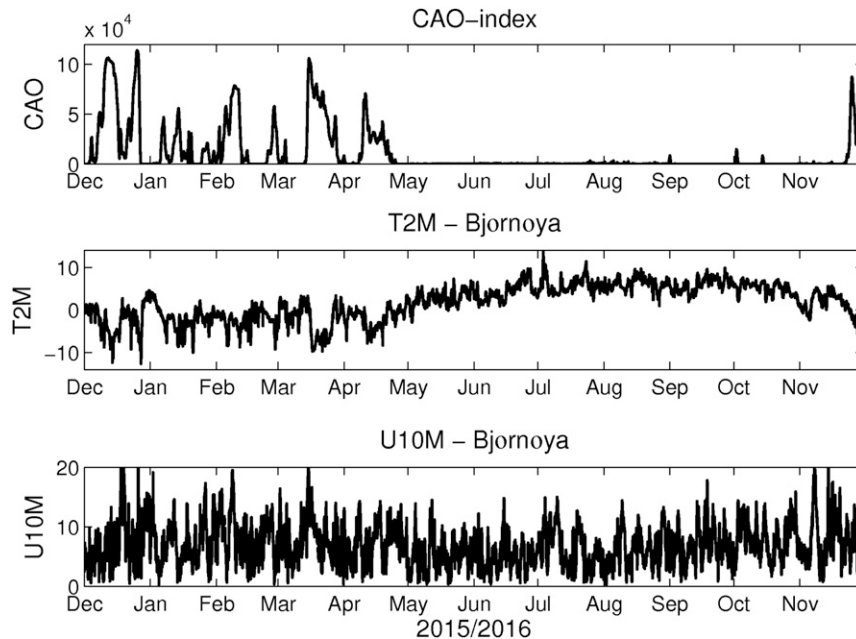
FIG. 3. (top) Time series of the CAO index [number of grid points in AROME-Arctic where the CAO index, defined in Papritz et al. (2015), is larger than 4]. The observed (middle) T2M and (bottom) U10M at the Bjørnøya surface observation site.

shown in Fig. 3, are from the Bjørnøya observation site, which is located in the southeastern corner of the CAO index region (Fig. 1). By comparing the major CAO events in the time series with the wind and temperature observations, we can see that the most abrupt temperature changes and strongest winds coincide with larger CAO index values. Similar correlations can be found for other observation time series in the European Arctic.

a. Surface

A set of 89 synoptic observations (Fig. 1) and continuous time series of model forecasts, which are initialized at 0000 and 1200 UTC and have lead times of 6, 9, 12, and 15 h, are used for verification. The observations are 3-hourly 2-m temperature (T2M) and 10-m wind speed (U10M) from the Norwegian synoptic station network. For the verification of T2M, a height correction [0.65 K (100 m)$^{-1}$ altitude] is applied to account for the different model resolutions and respective heights of the model's topography. The averaged (over all stations) root-mean-square error (rmse) is shown for the verification period with a running mean filter (20-day window) (Fig. 4). Since the rmse also depends on the variability of the signal in the observations and models, we computed the standard deviation from all records. However, we found that the standard deviation is 7.7 K for the observations and in between 7.4 and 7.6 K for the model systems. The rmse of all models is larger during the winter months (October–May)

for both T2M and U10M, which is expected from the seasonal changes of the wind and temperature variability (Fig. 3). A sharp transition in the wind rmse, from about 3 to 2 m s^{-1}, is visible at the end of April for all model systems. This transition cannot originate from the model system updates in March 2016, since the transition also exists for ERA-Interim, which has not been modified since its entry into service.

For the rmse of the T2M there is a clear separation of the AROME-Arctic model from the other model systems. The differences are largest in winter and about 1 K. HRES shows consistently lower rmse values than ENS and ERA-Interim throughout the year. After the model updates in March 2016, the rmse results of ENS are smaller than those of ERA-Interim; however, the differences between those two model systems are small.

In a spatial comparison of the T2M rmse and bias, in between the AROME-Arctic and HRES model, we further divide the results into observed T2M below and above −10°C (Figs. 5 and 6). The division into these two temperature ranges follows the analysis of Atlaskin and Vihma (2012), who found that in Nordic regions HRES and AROME have the largest positive bias during cold conditions (T2M < −10°C), which is often caused by temperature inversion and is underestimated in the models. Indeed, largest positive model bias is found in cold conditions. Especially, at the weather stations located farther inland, HRES shows a strong positive
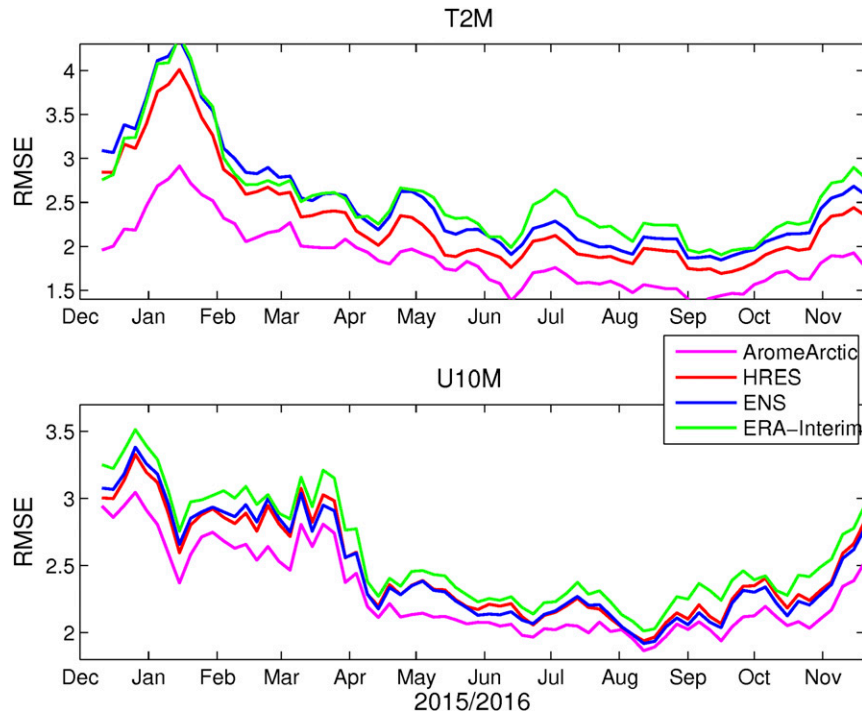
FIG. 4. Time series (running mean) of the rmse values of (top) T2M and (bottom) U10M analyzed at 89 surface observation sites shown in Fig. 1 for AROME-Arctic (magenta), HRES (red), ENS (blue), and ERA-Interim (green) are shown.

model bias (larger than 4 K). For stations closer to the coast, the bias of HRES is predominantly negative. In AROME-Arctic the T2M bias is about 1–2 K for T2M higher than −10°C and it varies between −2 and +2 K for T2M below −10°C. In the northern areas (Bjørnøya and the Svalbard Archipelago), the forecast skill of the models is similar. The reason for this could be attributed to issues related to the representation of ocean and sea ice surface properties (see also section 5), which cancel out the benefits gained from the higher resolution.

The rmse values for T2M lower than −10°C are very similar between AROME-Arctic and HRES, with values of 5 K in the inland and 2–4 K closer to the coast. For T2M higher than −10°C, HRES shows largest rmse values closer to the coast with values of up to 4 K, while AROME-Arctic has rmse values predominantly of around 2–3 K.

The standard deviation of U10M is $3.5 \, \text{m s}^{-1}$ for the observations and $3.3 \, \text{m s}^{-1}$ for AROME-Arctic. The ECMWF model systems show significantly lower standard deviations with values between 2.7 and $2.8 \, \text{m s}^{-1}$. Although a larger standard deviation also increases the rmse, AROME-Arctic still has smaller rmse values than the global systems throughout the entire 1-yr period. Interestingly, the rmse values of HRES and ENS are very similar, although the models have different horizontal and vertical resolutions. ERA-Interim has the largest

rmse throughout the entire year. In Fig. 7 the spatial maps of wind rmse and bias of AROME-Arctic and HRES are shown for the wintertime. In the region of the Svalbard Archipelago the wind rmse is smaller by about $1 \, \text{m s}^{-1}$ for HRES and, further, the wind bias for HRES is generally negative (-3 to $-1 \, \text{m s}^{-1}$), whereas it is positive for AROME-Arctic ($1–3 \, \text{m s}^{-1}$). The coastal areas of the Norwegian mainland show the largest differences between AROME-Arctic compared to HRES, for both rmse and bias, with differences of about $2 \, \text{m s}^{-1}$. Again, the wind bias for HRES is mainly negative, whereas AROME-Arctic shows positive and negative values.

b. Upper air

We analyze observational records from three radiosonde sounding stations, which are all located within the AROME-Arctic model domain. Ny Ålesund is the most northward station and located on Svalbard, whereas Bjørnøya is an island between the Svalbard Archipelago and the Norwegian mainland, and Jan Mayen is an island between Iceland and Svalbard. The three weather stations are marked by green dots in Fig. 1. The radiosonde data are not independent, in the sense that it is assimilated in all of the evaluated model systems.

In the following, we present two separate upper-air analyses. First, a pressure-level-based verification is performed
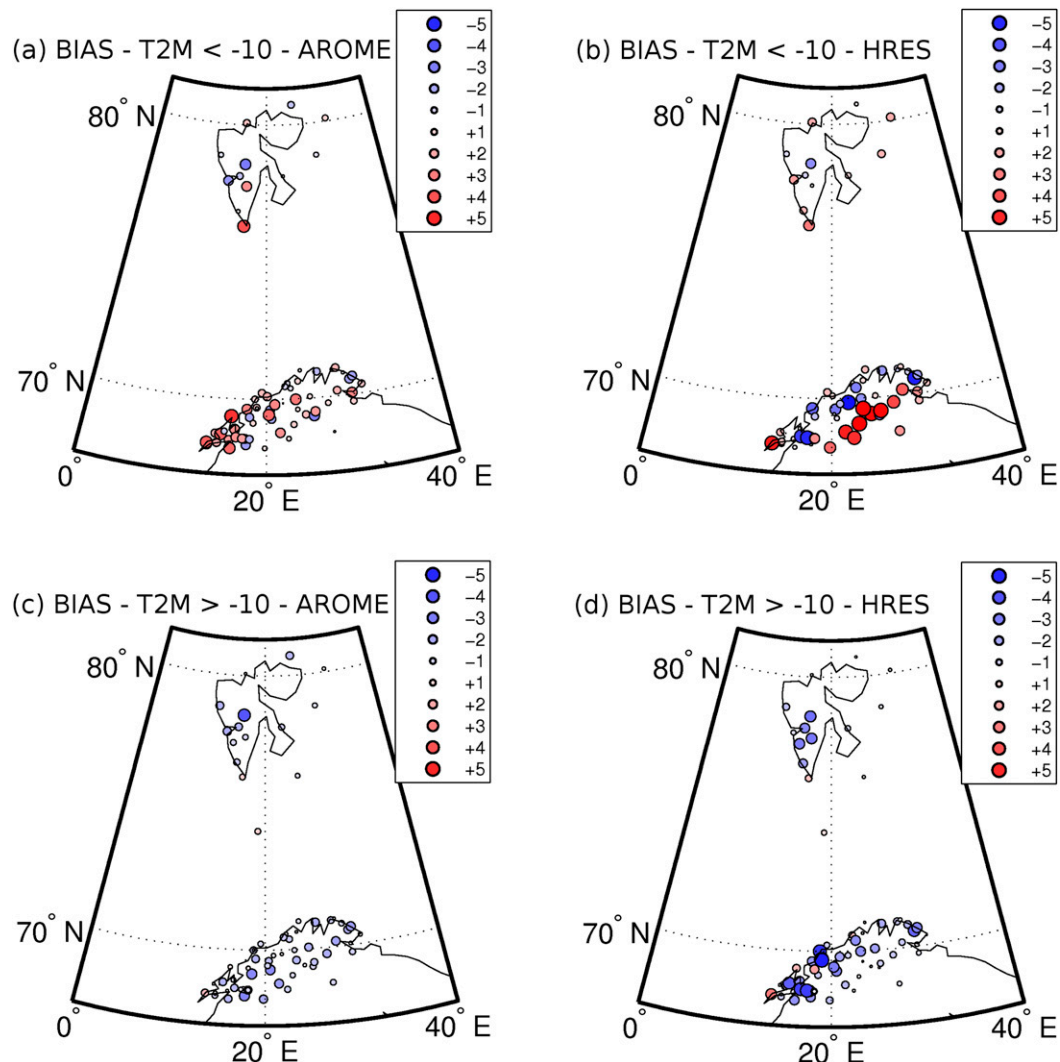
FIG. 5. The bias T2M computed for the period 1 Dec 2015–15 Mar 2016. Results are divided into cases, where T2M < −10°C and T2M > −10°C, for (a),(c) the AROME-Arctic model and (b),(d) HRES.

with pressure levels ranging from 950 to 50 hPa. The observation dataset has been obtained from the NOAA/ESRL Radiosonde Database (www.esrl.noaa.gov/raobs/). Second, the lowest atmospheric layer (10–300 m) is analyzed; therefore, the raw radiosonde data and the model output are interpolated onto a z-level grid for altitudes from 10 to 300 m. All radiosonde data are compared against forecasts of 12-h lead time and analysis times at 0000 and 1200 UTC.

The upper-air temperature and wind verification are shown for the two stations, Bjørnøya and Jan Mayen (Fig. 8). Below the 50-hPa pressure level the temperature bias for all models is below 0.3 K, whereas ERA-Interim has the smallest values in between 300 and 900 hPa. The temperature rmse for all models is around 1 and 2 K for Bjørnøya and Jan Mayen, respectively. The

rmse values peak at around 850 and 200 hPa at both weather stations. The upper peak, in the height of the tropopause, is also visible in the analyses of Bromwich et al. (2016). At Jan Mayen all models have very similar rmse and bias values, whereas at Bjørnøya HRES and ENS have the smallest rmse values and almost no differences between the models is visible. AROME-Arctic has lower rmse values compared to ERA-Interim only in the two lowest levels (925 and 1000 hPa) at Bjørnøya. In general, for both locations, the largest differences in between the models for temperature rmse and bias are in the levels closest to the surface.

The similarities between AROME-Arctic, HRES, and ENS at Jan Mayen are most likely due to the proximity of the (most common inflow) lateral boundaries. The reason for the increased rmse at Bjørnøya
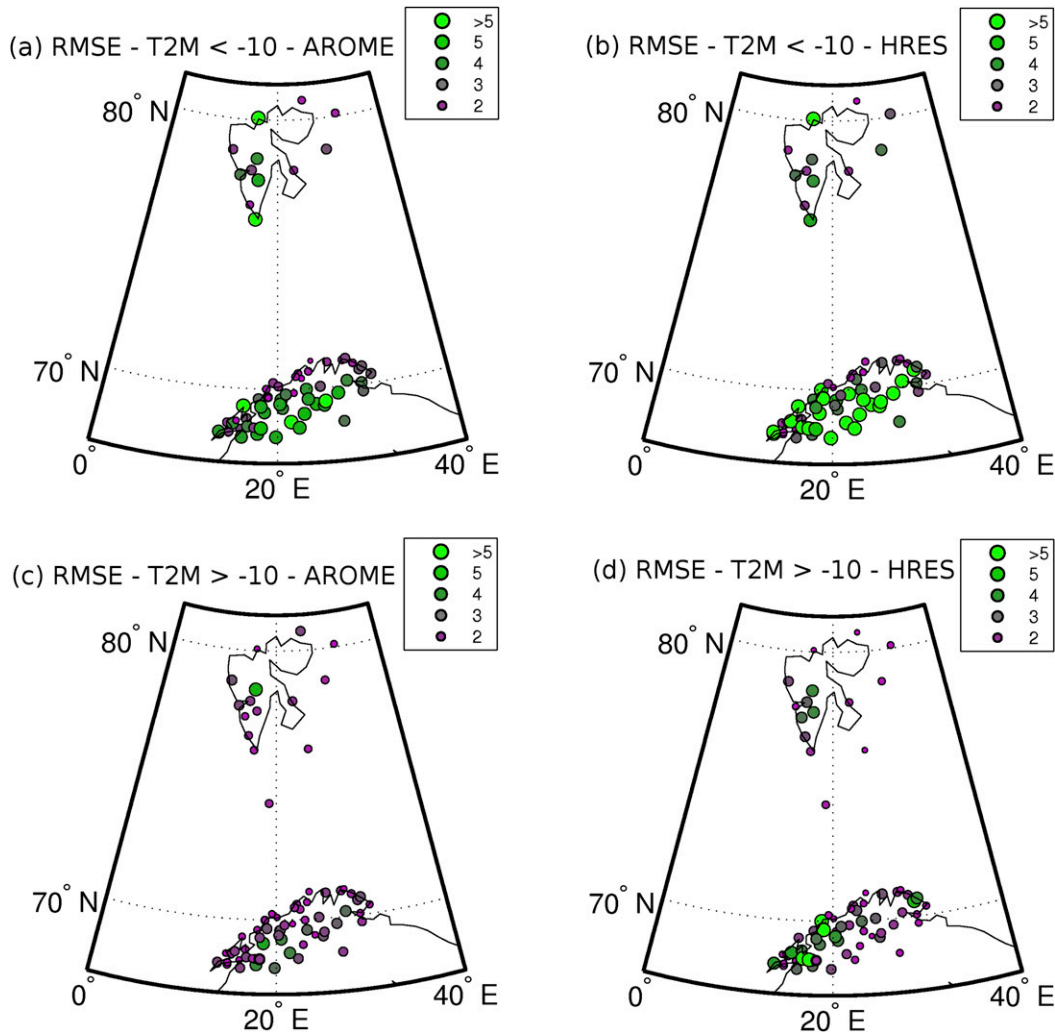
FIG. 6. The rmse T2M results computed for the period 1 Dec 2015–15 Mar 2016. Results are divided into cases, where T2M < −10°C and T2M > −10°C, for (a),(c) the AROME-Arctic model and (b),(d) HRES.

should be investigated further. It might be related to the initialization process with 3DVAR assimilation in combination with large-scale mixing of 6-h-old HRES data (Müller et al. 2017), the influence from 6-h-old lateral boundary conditions from HRES, or the presence of more small-scale features typically increasing the rmse.

The rmse for wind is between 2 and 5 m s^{-1}. The rmse peaks at about 300 hPa, which coincides with the height of the strongest upper-level winds (average values of around 20 m s^{-1}) and the polar jet stream, consistently with the radiosonde verification of Bromwich et al. (2016). All models have very similar rmse values. The wind bias is negative above the lowest level (1000 hPa), with values below 1 m s^{-1}. At Bjørnøya, ERA-Interim has the largest negative bias. The largest differences in wind bias in between the models are in the lowest level (1000 hPa), and for Jan Mayen, all models have a

positive bias in the lowest level with values of up to 1.8 m s^{-1}.

The radiosonde verification of the lower 300 m of the atmosphere is shown for the Ny Ålesund station (Fig. 9). We are specifically interested in the representation of the stable boundary layer and only include time steps in the analysis, where the lower 100 m of the atmosphere is stable stratified. The stability is determined from the observed potential temperature profile. In total, around 250 time steps are utilized for the analysis. The mean observed and forecasted profiles of temperature and wind show that in the lower 50 m above the surface the mean observed temperature increases slightly with height, which is not visible in the models' forecasts (Fig. 9). The temperature bias is smallest for AROME-Arctic (around 0.5 K) and largest for ERA-Interim (up to 2 K). The temperature rmse values of all the
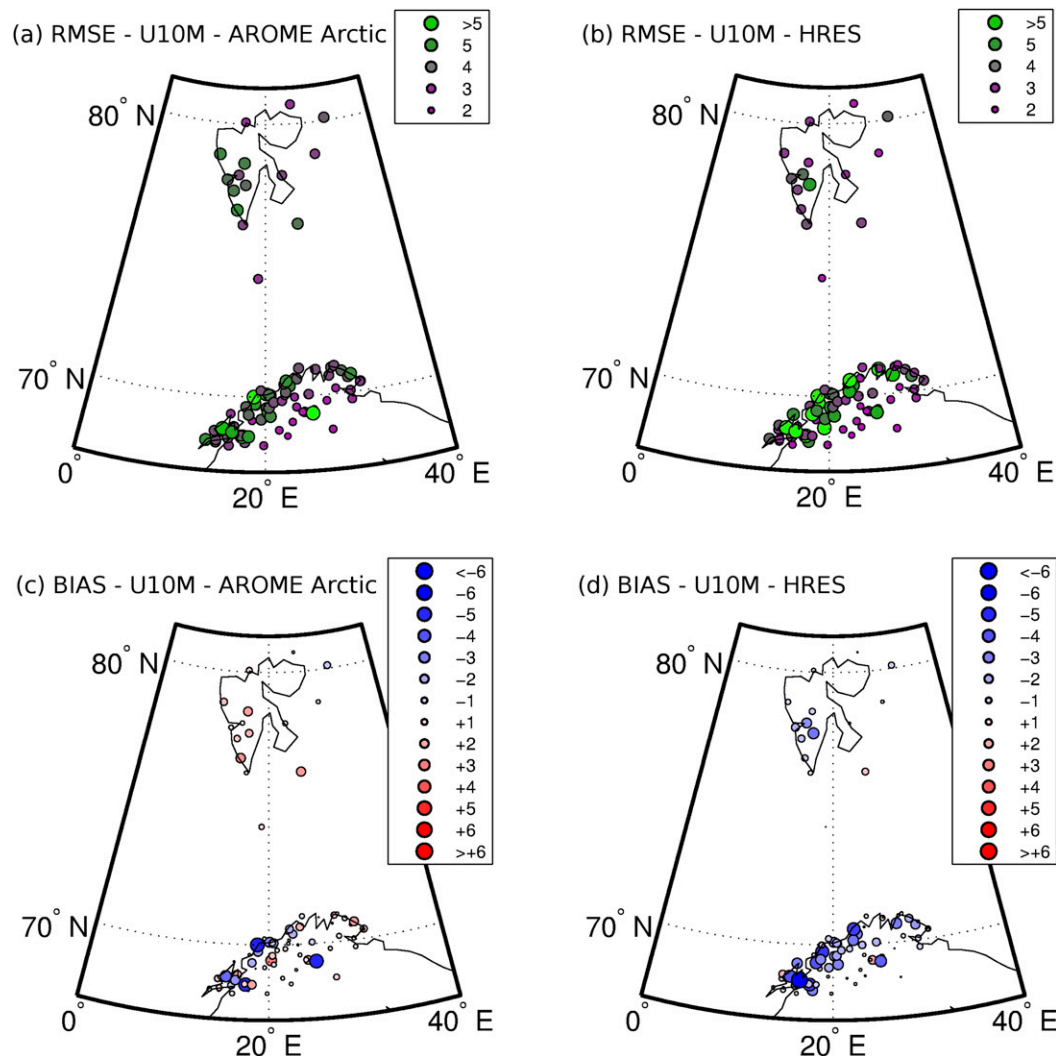
FIG. 7. The rmse and bias of U10M computed for the period 1 Dec 2015–15 Mar 2016 for (a),(c) the AROME-Arctic model and (b),(d) HRES.

models are largest in the lower 50–100 m with values of up to 2 K, whereas at heights of 100–300 m the rmse values are about 1 K smaller.

The shape of the mean wind profile of AROME-Arctic is similar to the observed results, but with a positive bias of around 1 m s^{-1}. The mean observed boundary layer thickness is about 100 m. In AROME-Arctic this seems to be well represented; however, in all of the global models the boundary layer thickness is much larger at about 300 m or even thicker. This is an indication of a too diffusive boundary layer in the ECMWF models (Viterbo et al. 1999; Beljaars 2001). The wind bias of the ECMWF models is in between 0 and 2 m s^{-1} in the lower 300 m of the atmosphere. The wind rmse values for all models increase with height and are 3–4 m s^{-1} in all models.

4. Representation of a polar low and strong winds

In addition to the rmse and bias verification in the previous section, an important characteristic of a forecasting system is the ability to predict high-impact weather conditions. In the European Arctic polar lows are frequently observed. They develop over the open sea (e.g., Blechschmidt 2008; Noer et al. 2011) and, although they dissipate quickly after landfall, their small scales and fast development often put human life and property, as well as the natural environment, at great risk.

CAOs, polar lows, and in general the largest wind variability and maxima are observed during the winter months (Fig. 3). Hence, before we analyze one specific polar low case in the Norwegian Sea, we first compare the spatial distribution of the 95th percentile wind speed
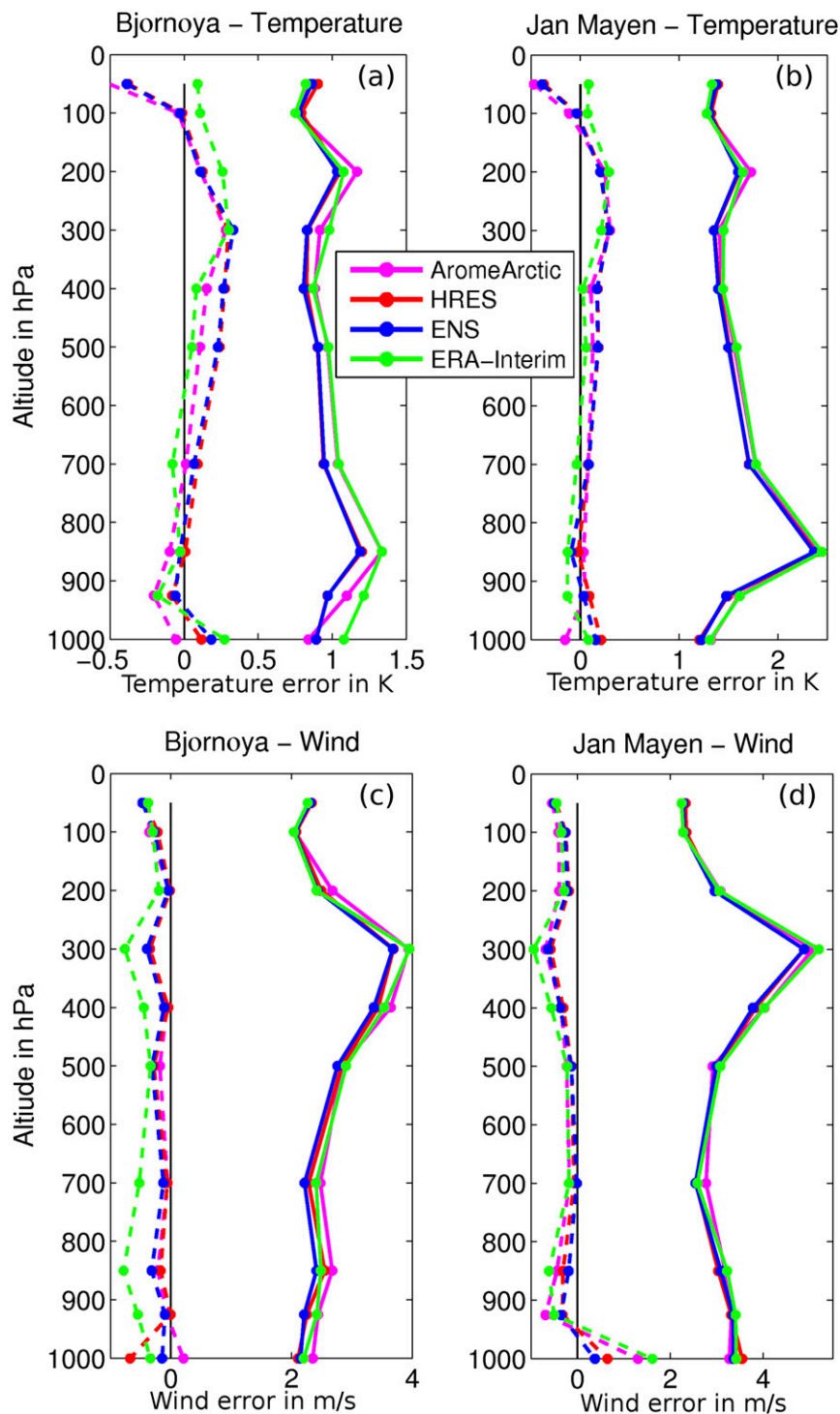
FIG. 8. The rmse (solid lines) and bias (dashed lines) of upper-air evaluations at pressure levels between 1000 and 50 hPa. Evaluation is performed for a 1-yr period and with radiosonde observations from the Bjørnøya and Jan Mayen weather stations. The 12-h forecasts of AROME-Arctic (magenta), HRES (red), ENS (blue), and ERA-Interim (green) are evaluated against (a),(b) temperature observations and (c),(d) wind observations.
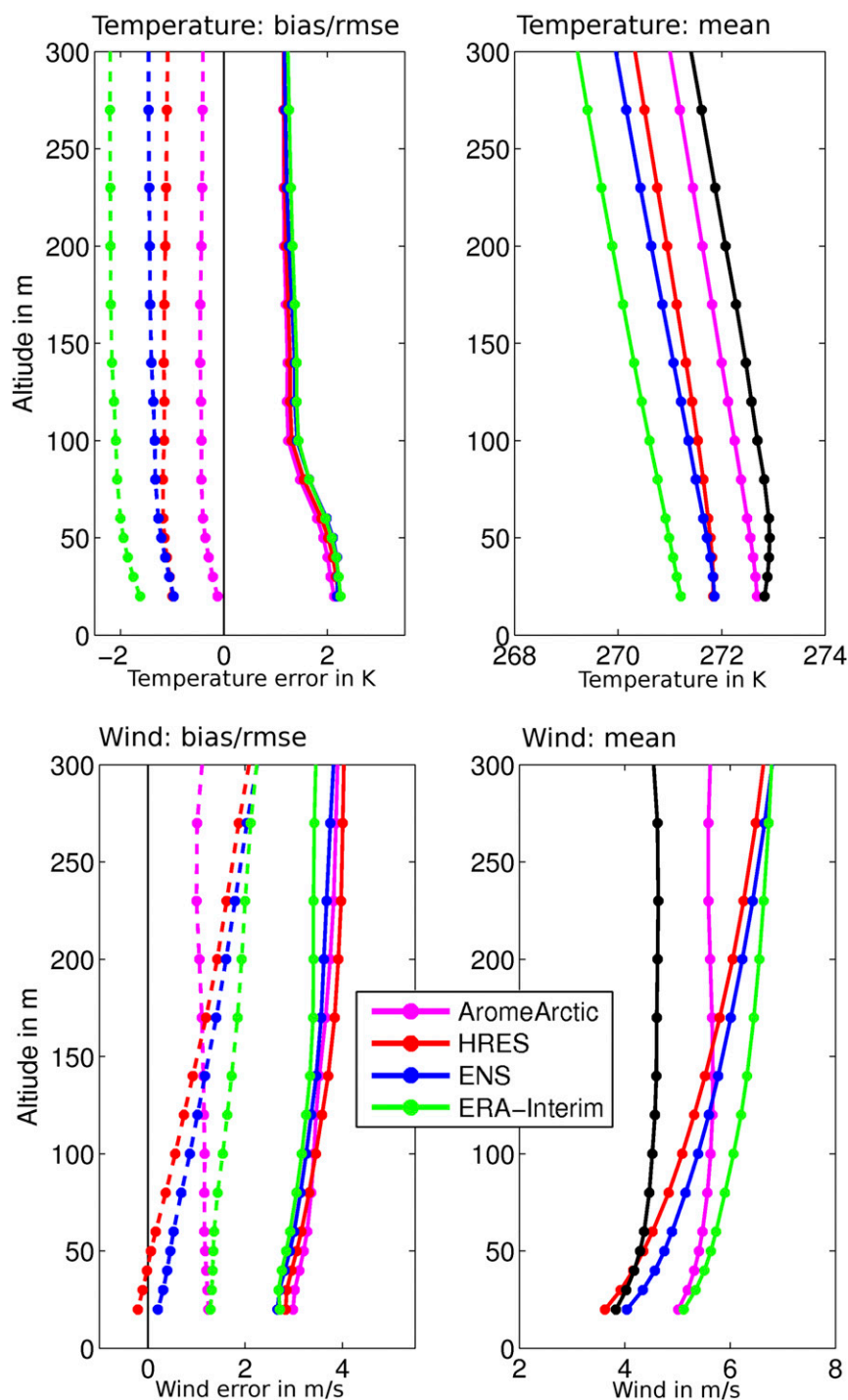
FIG. 9. Evaluation of the lower atmosphere (0–300-m altitude) with radiosonde observations from the Ny Ålesund weather station. The evaluation is performed during stable atmospheric conditions in the lower 100 m, determined from the observed potential temperature. (left) The rmse (solid lines) and bias (dashed lines) results for (top) temperature and (bottom) wind are shown. (right) The mean profiles of (top) temperature and (bottom) wind are shown. The black solid line represents the observations.
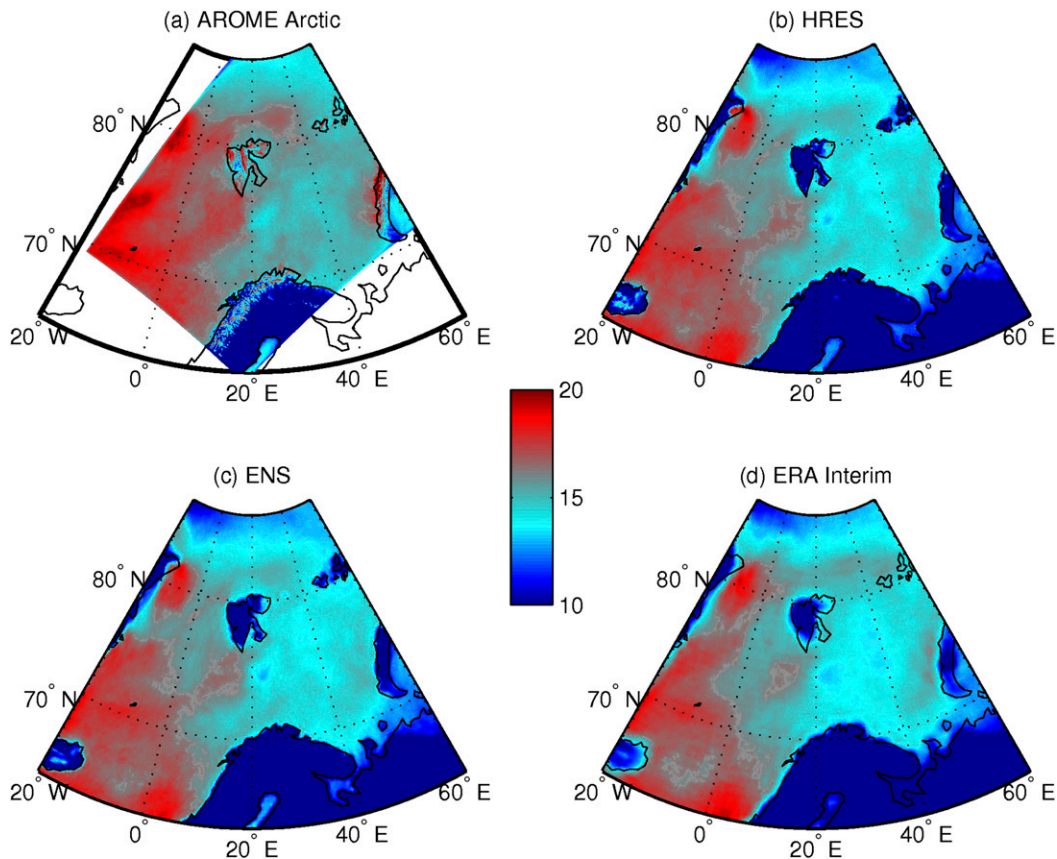
FIG. 10. The 95th percentile of U10M wind in (a) AROME-Arctic, (b) HRES, (c) ENS, and (d) ERA-Interim. The statistics are performed for the time from 1 Dec 2015 to 30 Mar 2016.

(P95) in between all analyzed model systems (Fig. 10). The results show that wind extremes are largest in AROME-Arctic with P95 values of up to 20 m s^{-1}. The ECMWF models show P95 values below 20 m s^{-1} and, in general, the global models have very similar characteristics despite their different spatial resolutions. Most pronounced differences between AROME-Arctic and the ECMWF models are in coastal areas of the Norwegian mainland and over Svalbard, where AROME-Arctic has values of up to 20 m s^{-1} and the ECMWF systems have values of 10 m s^{-1} and below. Over the ocean areas, in the northern part of the Norwegian Sea and along Novaya Zemlya Island the model systems are different in their representations of high wind speeds, as well. There, AROME-Arctic shows again values of up to 20 m s^{-1}, while the ECMWF systems have values of around 15 m s^{-1}.

On 8 December 2016 a low formed northeast of Jan Mayen and intensified as it moved southeastward toward the coast of Finnmark in northern Norway. The low was initially not termed a polar low since the air mass in which it formed was not very unstable. Soundings only showed

instability up to approximately 700 hPa, whereas 500–400 hPa is regarded as the normal for polar lows. There were instead several other dynamical factors involved. The polar low developed from an open wave that was embedded in a northwesterly jet flowing across Greenland, and in a later stage it exited the jet on the cold north side (left jet exit; Brümmer et al. 2009). This is a formation pattern that favors rapid intensification. Furthermore, it followed a sharp baroclinic zone at the southwestern edge of an upper cold core throughout its life-span. At the time of landfall (between 1800 and 2400 UTC) it arrived into an area of deeper instability, and there it took on the shape of a large polar low.

A visual comparison of forecasted winds in between the AROME-Arctic and HRES shows that the forecasted polar low locations (30-h lead time) of the two systems are very similar and are consistent with satellite observations (not shown). To analyze the wind characteristics of the model systems, we compare wind speeds of the very short-range forecasts (6-h lead time) of AROME-Arctic and HRES with the Advanced Scatterometer (ASCAT) level 2 wind product (Fig. 11).
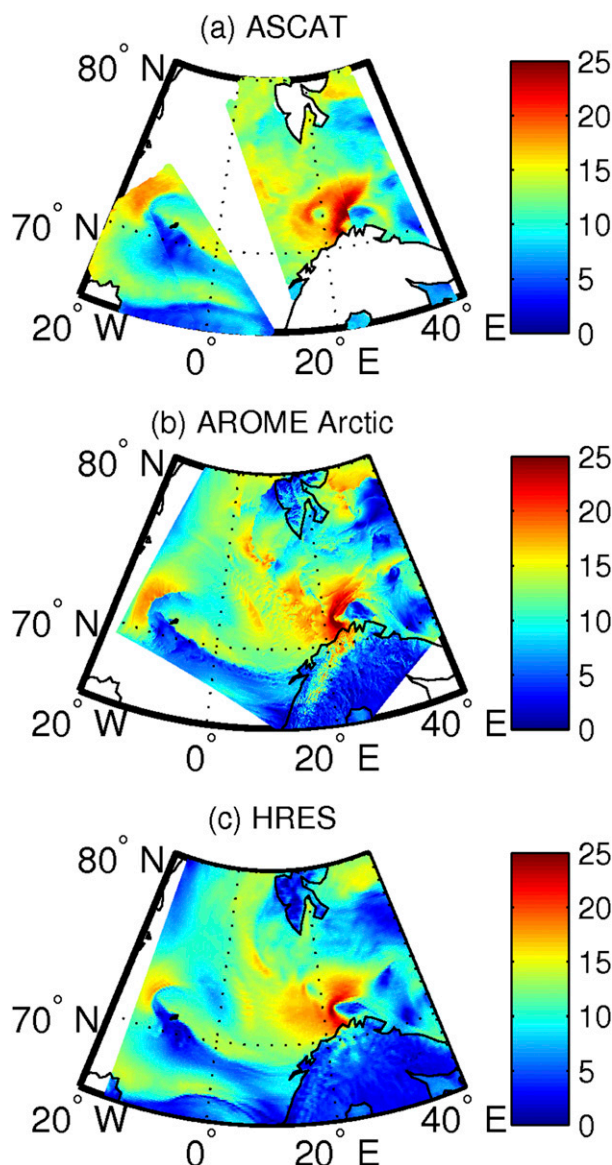
FIG. 11. Polar low close to the Norwegian coast at 1800 UTC 8 Dec 2016. (a) The 10-m wind speed of two tracks (approximately 1 h apart) from the level 2 ASCAT 12.5-km resolution product. The 6-h forecasts (with analysis time at 1200 UTC 8 Dec 2016) of 10-m wind speed from (b) AROME-Arctic and (c) HRES.

Two satellite passages of the ASCAT winds are shown, which are approximately 1 h apart. The wind patterns associated with the polar low are well represented in both model systems. Note, both model systems assimilate ASCAT winds.

Because of the mix of dynamical forcing (left jet exit) the low caused very strong winds across the Norwegian mainland. The synoptic observations from Fruholmen lighthouse on the Finnmark coast gave 10-m sustained winds of $29 \, \mathrm{m \, s^{-1}}$ with gusts of $37 \, \mathrm{m \, s^{-1}}$. This makes this

low one of the 5% strongest polar lows recorded since 2000. Maximum observed wind speeds associated with this polar low and along the Norwegian coast were about 25–$30 \, \mathrm{m \, s^{-1}}$. A comparison between AROME-Arctic and HRES shows that the landfall locations (i.e., areas of largest wind speeds) are well predicted by both models (Fig. 12). For HRES, the wind speeds are generally underestimated and only at a few locations are they larger than $20 \, \mathrm{m \, s^{-1}}$. In AROME-Arctic the maximum wind speeds along the coast are consistent with the observations. Farther inland, AROME-Arctic underestimates, however, it still shows more consistent results than HRES.

5. Challenges in the surface representation

In AROME-Arctic the largest part of the model domain is covered by ocean and sea ice. In the following, we discuss the state of the art of describing sea ice and ocean characteristics in (convective scale) Arctic weather prediction systems and, further, highlight some important features that are currently not available.

Sea ice is described in AROME-Arctic by using satellite sea ice concentration from the OSI-SAF satellite product (Tonboe et al. 2016). The effective resolution of this dataset is about 10–20 km. While the sea ice temperature is dynamically modeled by a 1D sea ice model, the sea ice concentration stays constant during the forecast (BKH). Furthermore, the representation of sea ice concentration in the model does not allow for small-scale structures in the sea ice (e.g., sea ice leads) but rather represents smoothed sea ice characteristics, as for example illustrated in Fig. 13.

The representation of sea ice leads is specifically important in the marginal ice zone (MIZ) and multiannual statistics show that sea ice lead frequencies are largest in the areas of the Fram Strait and Barents Sea (Willmes and Heinemann 2016). The sea ice conditions, at the start of and during (after 4 days) a CAO event in March 2016, are illustrated by the OSI-SAF sea ice concentration product, by the MODIS-based satellite product of sea ice leads (Willmes and Heinemann 2015), and by a mosaic of Synthetic Aperture Radar (SAR) images. The latter is a novel product from the European satellites *Sentinel-1A* and *-B*, and 43 scenes with SAR data in HV polarization obtained in extra-wide mode with spatial resolution of 100 m were obtained from the Copernicus Open Access Hub for two periods of times: 18–19 March and 23–24 March 2016. Calibration of normalized radar cross sections and removal of thermal and scalloping noise from SAR data were performed using the method developed by (Park et al. 2017). A mosaic of SAR images on a regular grid of a geographic projection was
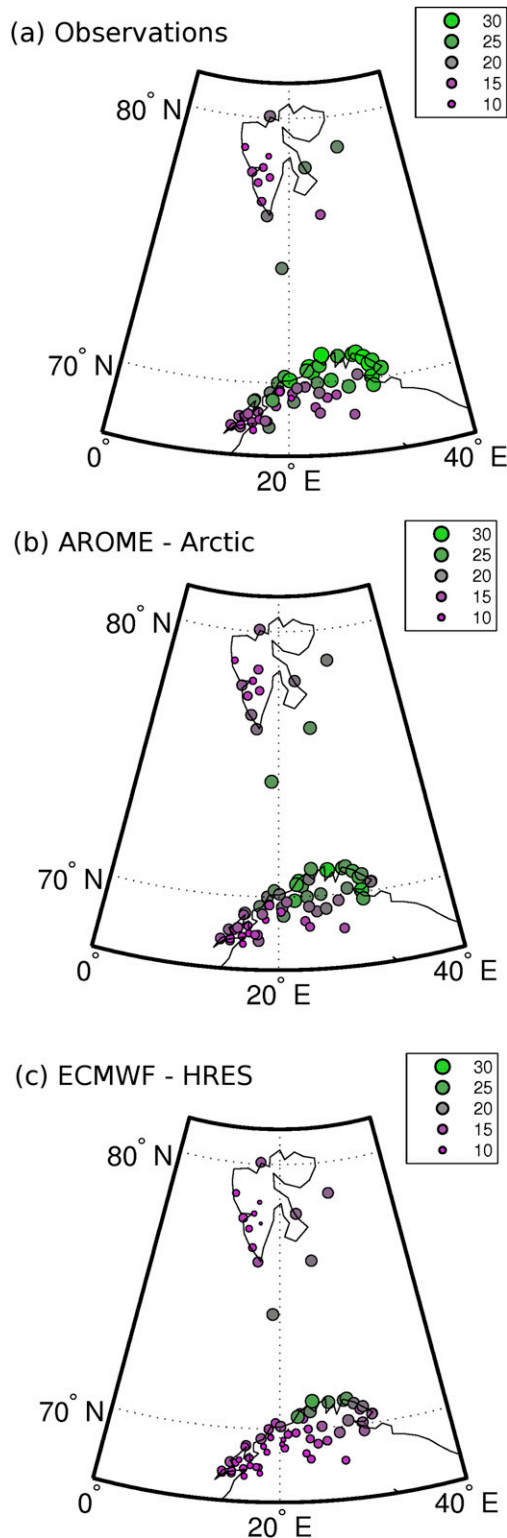
FIG. 12. The maximum winds observed within the period from 0000 UTC 8 Dec to 0012 UTC 9 Dec 2016. In (a) from synoptic 10-m wind observations and from forecasts at analysis time 1200 UTC 7 Dec 2016 from (b) AROME-Arctic and (c) HRES.

created using open-source Nansat software (Korosov et al. 2016).

During the CAO a large-scale drift of the sea ice cover in a southward (southwestward) direction toward the Svalbard Archipelago is visible in all products (Fig. 13). Also, the OSI-SAF sea ice drift product (Lavergne 2016) shows a southward sea ice drift of more than $10 \, km \, day^{-1}$ (not shown). The sea ice lead structure, as seen in the MODIS product, shows large sea ice leads (or openings) of $O(10–100)$ km, which quickly change their characteristic structure during the CAO. A consistent structure of leads and their changes is also visible in the SAR images. Apparently, sea ice leads are dominant in the entire domain shown in Fig. 13 and not only in the MIZ. We conclude that those sea ice lead structures and the dynamics on short time scales are relevant for a 2.5-km-resolution atmospheric model. The fast changes of sea leads, induced by the strong winds during CAOs, might provide for an important feedback mechanism to the atmosphere, as a result of the associated changes in air–sea heat fluxes. The MODIS sea ice lead product is based on the thermal-infrared data of the MODIS sensor and the leads are identified by comparing the warm signature of the ocean (lead) in comparison to the colder thick and snow-covered sea ice. Thus, this strongly highlights the modified ocean heat fluxes in areas of sea ice leads.

SSTs range from 0° to 8°C in the AROME-Arctic domain and show fine structures and strong gradients. This is a result of the extension of the warm North Atlantic Current, which transports warm water masses toward high latitudes. Those structures are smoothed in the currently used satellite retrievals (Fig. 14). Higher-resolution products are currently only available from high-resolution ocean prediction systems. Although the spatial structures of high-resolution models are more realistic [e.g., the eddying recirculation of Atlantic water along the sea ice edge; Hattermann et al. (2016)], there are relatively large biases due to the lack of observational data on small spatial scales (Fig. 14).

To test the impact of the high-resolution representation of the ocean surface temperature on the model performance, we performed a model sensitivity experiment, where SST and sea ice concentration are initialized by an operational ocean forecasting system. The ocean system has a horizontal resolution of 4 km and is based on the Regional Ocean Modeling System (ROMS) model framework (Shchepetkin and McWilliams 2005; Debernard et al. 2017). The sensible heat fluxes, during the CAO described in the previous paragraphs of this section, with high-resolution and coarser-resolution SST are shown in Fig. 14. As expected, the heat fluxes show variations on higher spatial
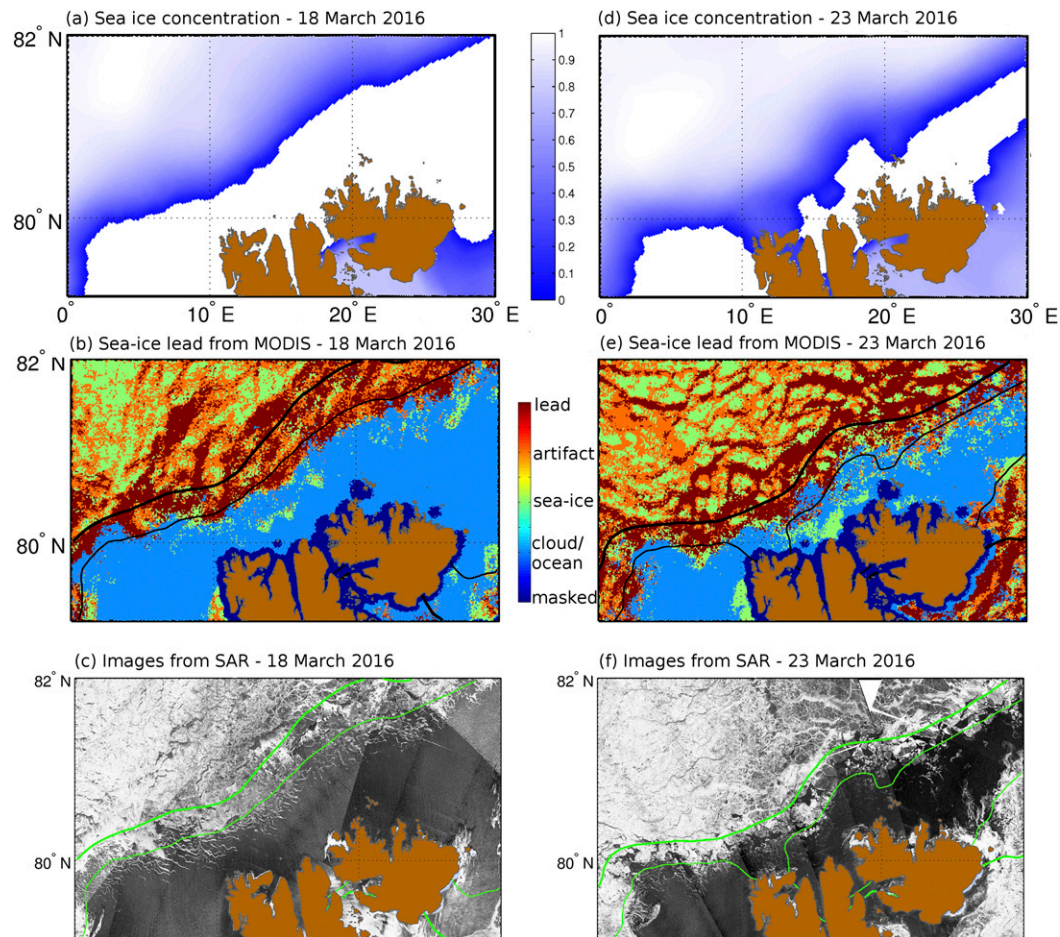
FIG. 13. Change of sea ice concentration and lead structures during a cold-air outbreak in March 2016. Conditions are shown for (left) 18 and (right) 23 Mar 2016. (a),(d) The OSI-SAF sea ice concentration products (regridded and postprocessed for use in AROME). (b),(e) Sea ice lead products based on MODIS satellite observations (red, lead; orange, artifact; green, sea ice; blue, cloud/ocean; dark blue, landmask). For more details see Willmes and Heinemann (2015). Black thick and thin lines represent 80% and 20% isolines obtained from OSI-SAF ice concentrations, respectively. (c),(f) Mosaics of SAR images (surface backward-scattering coefficient of radar wave). Green thick and thin lines represent 80% and 20% isolines obtained from OSI-SAF ice concentrations, respectively.

scales. In general, however, the use of the ROMS SST and sea ice concentration fields in the atmospheric forecasting system is leading to a degradation of the temperature forecasts compared to the operational system (not shown). We conclude that the bias of the simulated SST dominates and, thus, limits the expected improvements from the representation of the ocean mesoscale characteristics. High quality high-resolution SST data from satellites will be needed in the future, in order to provide the atmospheric model with SST data directly, or indirectly, via a constrained ocean model system.

6. Summary and conclusions

A detailed analysis of the representation of wind and temperature is performed with the regional convection-

allowing model system AROME-Arctic, as well as with different configurations (HRES, ENS, and ERA-Interim) of the global model system ECMWF IFS. Surface observations are taken from the Norwegian weather station network, which covers northern Norway, the Svalbard Archipelago, and some islands in the Nordic seas. The evaluation of the atmosphere above 10-m altitude is performed at three radiosonde observation sites. The focus of this study is on the summarized statistics of very short-range forecasts and without a detailed analysis of dependencies on the forecast range.

In general, the rmse values are largest during the winter months, when the variability of the winds and temperature is highest. The main improvement of the convective-scale model system, compared to the global ones, is found at the surface and in the representations of
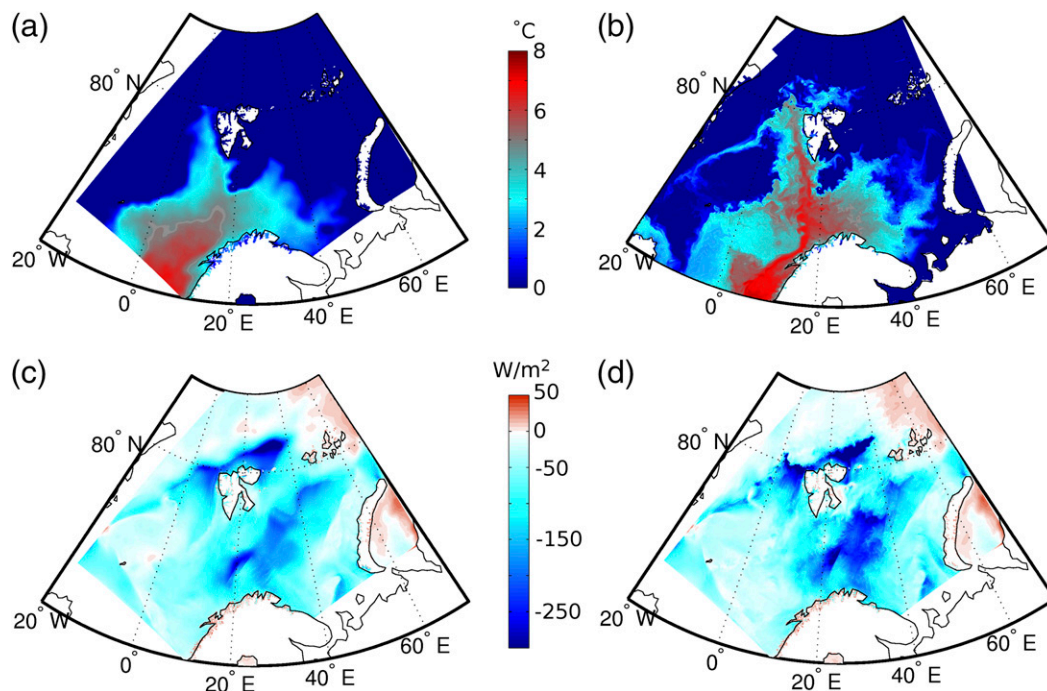
FIG. 14. Snapshot (1200 UTC 20 Mar 2016) of SST and turbulent heat flux over the ocean. The SSTs (a) of the OSTIA satellite product obtained as processed for AROME-Arctic and ECMWF model systems and (b) of the Norwegian Meteorological Institute's coupled ROMS–CICE (METROMS) ocean forecasting system (4-km horizontal resolution). The turbulent heat flux (in W m^{-2}) of the (c) operational AROME-Arctic system and (d) from a sensitivity experiment with high-resolution SST and sea ice concentration from the METROMS system.

the stable boundary layer. At the surface AROME-Arctic has a reduced bias and rmse compared to the global model systems. Those improvements are mainly visible across the Norwegian mainland, while the levels of forecast skill of AROME-Arctic and HRES are similar over the Svalbard Archipelago. The observed boundary layer thickness during stable atmospheric conditions is best represented by AROME-Arctic, while the ECMWF models have a too diffusive turbulence closure model that results in too deep boundary layers (Viterbo et al. 1999; Beljaars 2001). The upper-air evaluation shows that all model systems have similar characteristics in heights of 950–50 hPa.

Furthermore, the forecasts of a single polar low are analyzed. AROME-Arctic shows clear improvements in forecasting the landfall of a polar low and the associated extreme winds over the ocean and in coastal areas (up to 30 m s^{-1}). The results show that HRES underestimates the coastal extreme wind speeds during the landfall of the analyzed polar low. However, AROME-Arctic, HRES, and ENS have similar levels of skill, despite their different vertical and horizontal resolutions, in forecasting the location of a polar low, which is identified by a visual comparison of mean sea level pressure and ASCAT wind data.

The performed evaluation of the model systems has some limitations. The observation network in the northern part of the analyzed domain and over the ocean and sea-ice-covered areas is sparse, which implies that a generalization of the results is difficult. Most of the surface observation stations are on the Norwegian mainland and, thus, they might dominate some of the summary statistics. Furthermore, the surface observations are not assessed individually; that is, it could be of interest for future studies to classify specific observing stations, for example with respect to the station's representativeness, land–sea mask (model versus reality) and physiography. The wind bias of the AROME-Arctic model system compared to HRES showed some important differences in between the Svalbard Archipelago and the Norwegian mainland. It would be interesting for future studies to further analyze and understand the positive wind bias of the high-resolution model in the northern part of the domain. Also, it will be of interest to include more variables than wind and temperature, for example, humidity, cloud cover, and precipitation. Verification of precipitation forecasts would imply a careful use of snow-correction schemes and spatial verification methods, which will be part of future studies.

As a main challenge for convective-scale atmospheric modeling in the European Arctic, representations of the ocean and sea ice conditions are identified. Generally, sea ice initialization is a major issue for weather prediction (Smith et al. 2016) and the sea ice characteristics are a dominant constraint for atmospheric surface fluxes (Bourassa et al. 2013). The kilometer-scale structures of the sea ice can have strong effects on atmospheric conditions on short-time scales such as storm development and extreme convective events (Valkonen et al. 2008; Vihma 2014). Lüpkes et al. (2008) analyzed the effect of sea ice leads on the surface atmospheric boundary layer, by using a 1D atmospheric model coupled to a thermodynamic sea ice model. They concluded that under clear skies in winter a 1% change in the sea ice concentration can increase the T10M by up to 3.5 K. Within an operational context sea ice lead products are not available in real time or of sufficient quality. However, developments of satellite-based information on sea ice leads (Röhrs and Kaleschke 2012; Willmes and Heinemann 2015) and novel high-resolution sea ice model approaches (Rampal et al. 2016; Wang et al. 2016) are promising. Hence, we can expect significant advances in the realism of the sea ice representation for convective-scale weather prediction in the near future.

In addition, the SST products that are currently available are too coarse and do not represent the ocean small- and mesoscale characteristics. There are also gridded high-resolution products available, although with a significant amount of missing values as a result of cloud contamination. Thus, important small-scale feature with large temperature gradients are missing in the SST fields, which are available for operational weather prediction. New satellite-based SST products will soon be available (e.g., from the Sentinel-3 Sea and Land Surface Temperature Radiometer; www.sentinel.esa.int) and possibly a combination of the existing SST products could result in continuous high-resolution products, which could be used to assess their benefits for weather forecasting.

The improved sea ice and ocean surface representations will be important specifically during CAOs, where the small-scale sea ice characteristics change quickly as a result of strong winds. Furthermore, during CAOs the air–sea fluxes are largest because of the strong winds and large difference between the ocean and the cold atmospheric temperatures. Thus, an improved representation of ocean and sea ice will presumably improve forecasts and important dynamical features of CAOs, which can provide an important benefit for downstream weather conditions, such as the development of polar lows and even midlatitude weather.

REFERENCES

Atlaskin, E., and T. Vihma, 2012: Evaluation of NWP results for wintertime nocturnal boundary-layer temperatures over Europe and Finland. *Quart. J. Roy. Meteor. Soc.*, **138**, 1440–1451, https://doi.org/10.1002/qj.1885.

Bauer, P., and Coauthors, 2013: Model cycle 38r2: Components and performance. ECMWF Tech. Memo. 704, 58 pp., https://www.ecmwf.int/en/elibrary/7986-model-cycle-38r2-components-and-performance.

——, L. Magnusson, J.-N. Thpaut, and T. M. Hamill, 2016: Aspects of ECMWF model performance in polar areas. *Quart. J. Roy. Meteor. Soc.*, **142**, 583–596, https://doi.org/10.1002/qj.2449.

Beljaars, A. C. M., 2001: Issues in boundary layer parametrization for large scale models. *Proc. Seminar on Key Issues in the Parametrization of Subgrid Physical Processes*, Reading, United Kingdom, ECMWF, https://www.ecmwf.int/en/elibrary/8027-issues-boundary-layer-parametrization-large-scale-models.

Bengtsson, L., and Coauthors, 2017: The HARMONIE–AROME model configuration in the ALADIN–HIRLAM NWP system. *Mon. Wea. Rev.*, **145**, 1919–1935, https://doi.org/10.1175/MWR-D-16-0417.1.

Blechschmidt, A.-M., 2008: A 2-year climatology of polar low events over the Nordic Seas from satellite remote sensing. *Geophys. Res. Lett.*, **35**, L09815, doi:10.1029/2008GL033706.

Bourassa, M. A., and Coauthors, 2013: High-latitude ocean and sea ice surface fluxes: Challenges for climate research. *Bull. Amer. Meteor. Soc.*, **94**, 403–423, https://doi.org/10.1175/BAMS-D-11-00244.1.

Bromwich, D. H., A. B. Wilson, L.-S. Bai, G. W. K. Moore, and P. Bauer, 2016: A comparison of the regional Arctic System Reanalysis and the global ERA-Interim reanalysis for the Arctic. *Quart. J. Roy. Meteor. Soc.*, **142**, 644–658, https://doi.org/10.1002/qj.2527.

Brümmer, B., G. Müller, and G. Noer, 2009: A polar low pair over the Norwegian Sea. *Mon. Wea. Rev.*, **137**, 2559–2575, https://doi.org/10.1175/2009MWR2864.1.

Davies, H. C., 1976: A lateral boundary formulation for multi-level prediction models. *Quart. J. Roy. Meteor. Soc.*, **102**, 405–418, https://doi.org/10.1002/qj.49710243210.

Debernard, J., N. Kristensen, S. Maartensson, K. Wang, and G. Waagb, 2017: Metno/metroms: Intermediate release. Norwegian Meteorological Institute, accessed 2017, https://doi.org/10.5281/zenodo.290667.

Dee, D. P., and Coauthors, 2011: The ERA-Interim reanalysis: Configuration and performance of the data assimilation system. *Quart. J. Roy. Meteor. Soc.*, **137**, 553–597, https://doi.org/10.1002/qj.828.

Donlon, C. J., M. Martin, J. Stark, J. Roberts-Jones, E. Fiedler, and W. Wimmer, 2012: The Operational Sea Surface Temperature and Sea Ice Analysis (OSTIA) system. *Remote Sens. Environ.*, **116**, 140–158, https://doi.org/10.1016/j.rse.2010.10.017.

Emmerson, C., and G. Lahn, 2012: Arctic opening: Opportunity and risk in the high north. Chatham House-Lloyd's Risk Insight Rep., 59 pp., https://www.chathamhouse.org/publications/papers/view/182839.

Gutjahr, O., G. Heinemann, A. Preusser, S. Willmes, and C. Drue, 2016: Quantification of ice production in Laptev Sea polynyas and its sensitivity to thin-ice parameterizations in a regional climate model. *Cryosphere*, **10**, 2999–3019, https://doi.org/10.5194/tc-10-2999-2016.

Hattermann, T., P. E. Isachsen, W.-J. Von Appen, J. Albretsen, and A. Sundfjord, 2016: Eddy-driven recirculation of Atlantic water in the Fram Strait. *Geophys. Res. Lett.*, **43**, 3406–3414, doi:10.1002/2016GL068323.

Hines, K. M., and D. H. Bromwich, 2017: Simulation of late summer Arctic clouds during ASCOS with Polar WRF. *Mon. Wea. Rev.*, **145**, 521–541, https://doi.org/10.1175/MWR-D-16-0079.1.

Jung, T., and M. Leutbecher, 2007: Performance of the ECMWF forecasting system in the Arctic during winter. *Quart. J. Roy. Meteor. Soc.*, **133**, 1327–1340, https://doi.org/10.1002/qj.99.

——, and M. Matsueda, 2016: Verification of global numerical weather forecasting systems in polar regions using TIGGE data. *Quart. J. Roy. Meteor. Soc.*, **142**, 574–582, https://doi.org/10.1002/qj.2437.

——, and Coauthors, 2016: Advancing polar prediction capabilities on daily to seasonal time scales. *Bull. Amer. Math. Soc.*, **97**, 1631–1647, https://doi.org/10.1175/BAMS-D-14-00246.1.

Korosov, A., M. W. Hansen, K.-F. Dagestad, and A. Yamakava, 2016: Nansat: A scientist-orientated python package for geospatial data processing. *J. Open Res. Software*, **4** (1), e39, http://doi.org/10.5334/jors.120.

Lavergne, T., 2016: Low resolution sea ice drift product user's manual, version 1.8. OSI SAF Tech. Rep., EUMETSAT, 31 pp., http://osisaf.met.no/docs/osisaf_cdop2_ss2_pum-sea-ice-drift-lr_v1p8.pdf.

Lüpkes, C., T. Vihma, G. Birnbaum, and U. Wacker, 2008: Influence of leads in sea ice on the temperature of the atmospheric boundary layer during polar night. *Geophys. Res. Lett.*, **35**, L03805, https://doi.org/10.1029/2007GL032461.

Moore, G. W. K., D. H. Bromwich, A. B. Wilson, I. Renfrew, and L. Bai, 2016: Arctic System Reanalysis improvements in topographically-forced winds near Greenland. *Quart. J. Roy. Meteor. Soc.*, **142**, 2033–2045, https://doi.org/10.1002/qj.2798.

Müller, M., and Coauthors, 2017: AROME-MetCoOp: A Nordic convective-scale operational weather prediction model. *Wea. Forecasting*, **32**, 609–627, https://doi.org/10.1175/WAF-D-16-0099.1.

Noer, G., O. Saetra, T. Lien, and Y. Gusdal, 2011: A climatological study of polar lows in the Nordic Seas. *Quart. J. Roy. Meteor. Soc.*, **137**, 1762–1772, https://doi.org/10.1002/qj.846.

Papritz, L., S. Pfahl, H. Sodemann, and H. Wernli, 2015: A climatology of cold air outbreaks and their impact on air–sea heat fluxes in the high-latitude South Pacific. *J. Climate*, **28**, 342–364, https://doi.org/10.1175/JCLI-D-14-00482.1.

Park, J.-W., A. Korosov, M. Babiker, S. Sandven, and J. Won, 2017: Efficient thermal noise removal for Sentinel TOPSAR cross-polarisation channel. *Geophysical Research Abstracts*, Vol. 19, Abstract 12613, http://meetingorganizer.copernicus.org/EGU2017/EGU2017-12613.pdf.

Rampal, P., S. Bouillon, E. Ólason, and M. Morlighem, 2016: NeXtSIM: A new Lagrangian sea ice model. *Cryosphere*, **10**, 1055–1073, https://doi.org/10.5194/tc-10-1055-2016.

Röhrs, J., and L. Kaleschke, 2012: An algorithm to detect sea ice leads by using AMSR-E passive microwave imagery. *Cryosphere*, **6**, 343–352, https://doi.org/10.5194/tc-6-343-2012.

Seity, Y., P. Brousseau, S. Malardel, G. Hello, P. Bénard, F. Bouttier, C. Lac, and V. Masson, 2011: The AROME-France convective-scale operational model. *Mon. Wea. Rev.*, **139**, 976–991, https://doi.org/10.1175/2010MWR3425.1.

Shchepetkin, A. F., and J. C. McWilliams, 2005: The Regional Ocean Modeling System (ROMS): A split-explicit, free-surface, topography-following coordinate ocean model. *Ocean Modell.*, **9**, 347–404, https://doi.org/10.1016/j.ocemod.2004.08.002.

Smirnova, J., and P. Golubkin, 2017: Comparing polar lows in atmospheric reanalyses: Arctic System Reanalysis versus ERA-Interim. *Mon. Wea. Rev.*, **145**, 2375–2383, https://doi.org/10.1175/MWR-D-16-0333.1.

Smith, G. C., and Coauthors, 2016: Sea ice forecast verification in the Canadian Global Ice Ocean Prediction System. *Quart. J. Roy. Meteor. Soc.*, **142**, 659–671, https://doi.org/10.1002/qj.2555.

Tonboe, R., and J. LaVelle, R.-H. Pfeiffer, and E. Howe, 2016: Product user manual for OSI SAF global sea ice concentration, version 1.4. OSI SAF Tech. Rep., EUMETSAT, 21 pp., http://osisaf.met.no/docs/osisaf_cdop2_ss2_pum_ice-conc_v1p4.pdf.

Valkonen, T., T. Vihma, and M. Doble, 2008: Mesoscale modeling of the atmosphere over Antarctic sea ice: A late-autumn case study. *Mon. Wea. Rev.*, **136**, 1457–1474, https://doi.org/10.1175/2007MWR2242.1.

Vihma, T., 2014: Effects of Arctic sea ice decline on weather and climate: A review. *Surv. Geophys.*, **35**, 1175–1214, https://doi.org/10.1007/s10712-014-9284-0.

——, and Coauthors, 2014: Advances in understanding and parameterization of small-scale physical processes in the marine Arctic climate system: A review. *Atmos. Chem. Phys.*, **14**, 9403–9450, https://doi.org/10.5194/acp-14-9403-2014.

Viterbo, P., A. Beljaars, J.-F. Mahfouf, and J. Teixeira, 1999: The representation of soil moisture freezing and its impact on the stable boundary layer. *Quart. J. Roy. Meteor. Soc.*, **125**, 2401–2426, https://doi.org/10.1002/qj.49712555904.

Wang, Q., S. Danilov, T. J. Kaleschke, and A. Wernecke, 2016: Sea ice leads in the Arctic Ocean: Model assessment, interannual variability and trends. *Geophys. Res. Lett.*, **43**, 7019–7027, https://doi.org/10.1002/2016GL068696.

Willmes, S., and G. Heinemann, 2015: Pan-Arctic lead detection from MODIS thermal infrared imagery. *Ann. Glaciol.*, **56**, 29–37, https://doi.org/10.3189/2015AoG69A615.

——, and ——, 2016: Sea-ice wintertime lead frequencies and regional characteristics in the Arctic, 2003–2015. *Remote Sens.*, **8**, https://doi.org/10.3390/rs8010004.

WMO-PPP, 2013: WWRP Polar Prediction Project Science Plan, No. 1. World Meteorological Organization Tech. Rep., 69 pp.

Zappa, G., L. Shaffrey, and K. Hodges, 2014: Can polar lows be objectively identified and tracked in the ECMWF operational analysis and the ERA-Interim reanalysis? *Mon. Wea. Rev.*, **142**, 2596–2608, https://doi.org/10.1175/MWR-D-14-00064.1.